



Synthesis, structural, electrical and magnetic characteristics of Co–Cd spinel nano ferrites synthesized via sol-gel auto combustion method

M. H. Nasr^{1,2} · M. M. Elkholy^{1,3} · L. M. S. El-Deen^{1,3} · Gamal M. Turkey⁴ · M. Moustafa⁵ · A. A. EL-Hamalawy¹ · A. S. Abouhaswa^{1,6}

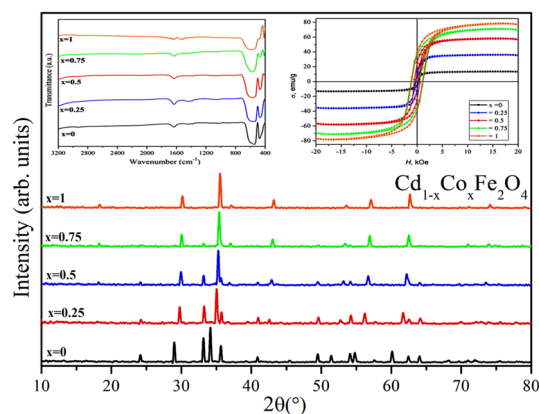
Received: 14 November 2023 / Accepted: 23 January 2024

© The Author(s), under exclusive licence to Springer Science+Business Media, LLC, part of Springer Nature 2024

Abstract

Nanocrystalline spinel ferrites with the general chemical formula $\text{Cd}_{1-x}\text{Co}_x\text{Fe}_2\text{O}_4$ (where $x = 0.0, 0.25, 0.75, \text{ or } 1.0$) were prepared using the sol-gel auto combustion method. To analyze the structural properties of the spinel ferrite samples that were manufactured, X-ray diffraction (XRD), scanning electron microscopy (SEM) and Fourier transform infrared spectroscopy (FTIR) were employed. A vibration sample magnetometer (VSM) and broadband dielectric spectroscopy (BDS) were used to examine the magnetic and dielectric properties of the synthesized ferrite samples. The principal cubic phase with space group $\text{Fd}\bar{3}\text{m}$ and hematite hexagonal phase $\alpha\text{-Fe}_2\text{O}_3$ were observed simultaneously, as determined by X-ray diffraction analysis. Rietveld refinement revealed that the lattice parameters and the volume fraction of the hematite hexagonal phase decreased as the concentration of Co dopant increased. Two unique absorption bands were recognized and their dependence on the concentration of Co was investigated and clarified with the use of FTIR analysis. According to VSM measurements, the saturation magnetization (M_s) and coercivity (H_c) were improved as the Co content increased. Through the examination of X-ray diffraction and magnetic characteristics, the cation distribution in $\text{Cd}_{1-x}\text{Co}_x\text{Fe}_2\text{O}_4$ spinel ferrite was explored. The pure cobalt ferrite sample exhibits the lowest permittivity and ac conductivity values, according to the dielectric measurements, reflecting the insulation feature of the pure cobalt ferrite.

Graphical Abstract



✉ A. S. Abouhaswa
aliabhaswa@hotmail.com

¹ Department of Physics, Faculty of Science, Menoufia University, Shebin El-Koom 32511, Egypt

² Faculty of Technological Industry and Energy, Delta Technological University, Quesna, Egypt

³ Physics Department, Faculty of Science, New Mansoura University, Dakahlia, Egypt

⁴ Department of Microwave Physics & Dielectrics, National Research Centre, Giza 12622, Egypt

⁵ Department of Physics, School of Science and Engineering, American University in Cairo, Cairo, Egypt

⁶ Institute of Natural Sciences and Mathematics, Ural Federal University, Ekaterinburg 620002, Russia

Keywords Spinel · Nano ferrites · Sol-gel · Cubic phase · Saturation magnetization · Cation distribution · Permittivity

Highlights

- Spinel ferrites nanocrystalline $\text{Cd}_{1-x}\text{Co}_x\text{Fe}_2\text{O}_4$ were prepared using sol-gel auto combustion method.
- X-ray diffraction revealed the presence of the main cubic phase with space group Fd3m.
- FTIR analysis was used to identify two distinct absorption bands.
- Magnetic measurements demonstrated that as the Co concentration increased; (M_s) and (H_c) improved.
- The conductivity spectra of the compositions show two different trends separated by a pronounced frequency.

1 Introduction

Spinel ferrite nanoparticles are one of the most significant magnetic oxides due to their well-known distinctive optical, electrical, and magnetic characteristics. This is particularly applicable considering the numerous technical uses for ferrites, including high density magnetic storage, sensors, biological drug delivery, broadband transformers, computer circuits, carrier telephony, and very effective catalysts [1–5]. The majority of these applications rely on these materials' magnetic characteristics, which may be attributed to a complex interaction of several elements with cationic distribution and spin canting being the most important and dominant [6–8].

Spinel ferrite is often denoted as MFe_2O_4 , where M symbolizes various transition metal elements. The substance under consideration contains M and Fe ions, which are found at either tetrahedral (A) or octahedral (B) interstitial sites. The use of spinel ferrite as a material for investigating the magnetic properties of nanoparticles is a subject of great interest [9]. In terms of the crystal structure of spinel ferrites, it has 56 atoms in total and a space group of Fd3m. 32 of these atoms are oxygen anions, which have a highly packed cubic configuration. The remaining atoms are metal cations, which are distributed across 8 out of the 64 available tetrahedral (A) sites and 16 out of the 32 available octahedral (B) sites [10–13].

The synthesis technique, additive substitution, and calcination procedure affect the ferrite's structure and physical characteristics [14–16]. The optical, electrical, dielectric, and magnetic characteristics of nanosized MFe_2O_4 may be effectively improved and controlled by doping with transition metal ions [17–19]. Doping spinel ferrite with transition metal ions modifies the distribution of cations between the tetrahedral (A) and octahedral (B) sites, resulting in various magnetic characteristics. Furthermore, the host matrices' microstructures can be controlled or doped with smaller divalent cations for enhancing electrical resistance [20]. The dopant ion can influence the free energy of the grain boundaries as well, functioning as a catalyst for grain development [21].

The cobalt spinel ferrite (CoFe_2O_4) is a magnetic material with well-known properties such as mechanical hardness, exceptional chemical stability, strong anisotropy, and

relatively high saturation magnetization (M_s) and coercivity (H_c). These properties are all associated with the cobalt spinel ferrite. The outcome is a plethora of applications, from microwave devices and high-density magnetic storage to sensors, broadband transformers, and digital circuits.

This study aims to synthesize Cd-Co spinel nano-ferrites, denoted as $\text{Cd}_{1-x}\text{Co}_x\text{Fe}_2\text{O}_4$ (in which $x = 0, 0.25, 0.5, 0.75, 1$); the synthesis method used is the sol-gel auto-combustion process. This study aims to enhance the structural, electrical, and magnetic properties of synthesized $(\text{Cd-Co})\text{F}_2\text{O}_4$ spinel nanoferrites by substituting Cd with Co. Additionally, a more precise characterization of spinel ferrite nanoparticles will be conducted using techniques such as X-ray diffraction (XRD), scanning electron microscopy (SEM), energy-dispersive X-ray spectroscopy (EDX), and Fourier-transform infrared spectroscopy (FTIR). Furthermore, the magnetic and dielectric characteristics of all samples were examined at room temperature. Therefore, the objective of the present study is to enhance the system's features in order to synthesize the "perfect" nano ferrite with distinctive characteristics that can be used to a variety of applications.

2 Experimental technique

2.1 Sample preparation

In this work, high-grade metal nitrates were employed to produce $\text{Cd}_{1-x}\text{Co}_x\text{Fe}_2\text{O}_4$ (in which $x = 0, 0.25, 0.5, 0.75, 1$) ferrite nanoparticles via a flash auto-combustion process. Cadmium nitrate $\text{Cd}(\text{NO}_3)_2 \cdot 6\text{H}_2\text{O}$ (99%) (LOBA CHEMIE), cobalt nitrate $\text{Co}(\text{NO}_3)_2 \cdot 4\text{H}_2\text{O}$ (99%) (CHEM-LAB), Ferric nitrate $\text{Fe}(\text{NO}_3)_3 \cdot 9\text{H}_2\text{O}$ (99%) (LOBA CHEMIE) and citric acid ($\text{C}_6\text{H}_8\text{O}_7$, 99%) (LOBA CHEMIE) have been utilized as the initial ingredients without additional processing. Various amounts of the starting components were utilized in accordance with the necessary stoichiometric proportions of the $\text{Cd}_{1-x}\text{Co}_x\text{Fe}_2\text{O}_4$. At room temperature, stoichiometric amounts of the nitrate precursors were dissolved in small quantities of distilled water, and citric acid was utilized as a fuel; molar ratio of metal nitrates to citric acid as (1:1). The resultant solution was blended using a

hotplate magnetic stirrer at 70 °C in order to ensure homogeneity, and the pH level was adjusted with ammonia to a value of ~7. In order to eliminate any excess water, the mixture was heated to approximately 95 °C while being constantly stirred. In the presence of ambient air, the brown gel spontaneously caught fire, producing a powdery light brown ash as an outcome. The samples of porous ash were ground into a fine powder and heated to 950 °C for annealing.

2.2 Samples characterization

The structure of the samples and their phase purity were analyzed at room temperature using X-ray diffraction measurements. A Bruker D8 Advance diffractometer equipped with $\text{CuK}\alpha$ radiation ($\lambda = 1.5418 \text{ \AA}$) was used for this purpose. The diffraction data were obtained by scanning 2θ values ranging from 5° to 70° at a scanning speed of 2°/min. The images for the examined samples were produced using a scanning electron microscope model Quanta 250 FEG (Field Emission Gun) connected to an EDX unit (Energy Dispersive X-ray Analyses) with a 30 kV accelerating voltage and a magnification range of 14 to 1,000,000. Image J software was applied to examine the SEM images. Fourier-transform infrared spectroscopy (FTIR) spectra of all the materials under investigation were obtained using a Perkin–Elmer 1430 infrared spectrometer; a wavenumber range of 200–4000 cm^{-1} was used for this analysis. A vibrating sample magnetometer (VSM) was employed to examine magnetic hysteresis characteristics in magnetic fields with intensities up to 25 kOe at room temperature. Dielectric investigations of samples were achieved using a Novocontrol high-resolution alpha analyzer in the frequency range 10^{-1} – 10^7 Hz at room temperature.

3 Results and discussion

3.1 X-ray diffraction

The X-ray diffraction (XRD) patterns of the spinel ferrite system $\text{Cd}_{1-x}\text{Co}_x\text{Fe}_2\text{O}_4$ ($x = 0.0, 0.25, 0.5, 0.75, 1.0$) after calcining at a temperature of 950 °C are shown in Fig. 1. The XRD patterns revealed that the existence of cubic-phase spinel ferrite with the space group Fd-3m. The principal lattice planes of the cubic spinel structure may be identified as (220), (311), (400), (422), (511), and (440). These lattice planes are significant in characterizing the cubic spinel structure. Additionally, it was observed that a second phase was present, except for the $\text{Co}_1\text{Fe}_2\text{O}_4$ sample. This second phase exhibited peaks corresponding to the hematite hexagonal phase $\alpha\text{-Fe}_2\text{O}_3$ (JCPDS#86-0550) with the R-3c space group. The incomplete diffusion of Cd ions

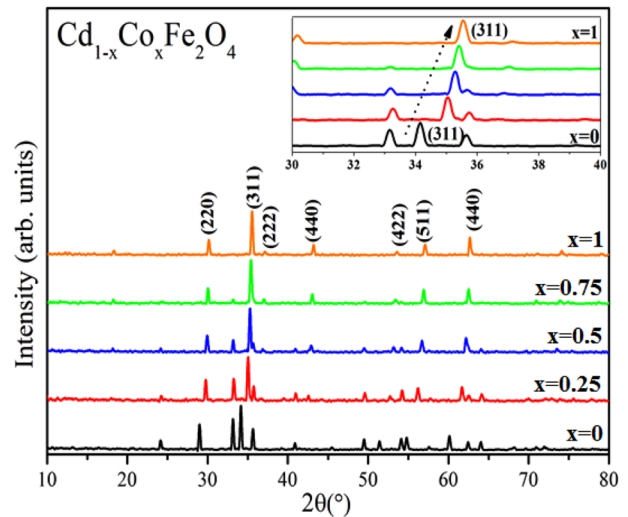


Fig. 1 X-ray diffraction patterns for the $\text{Cd}_{1-x}\text{Co}_x\text{Fe}_2\text{O}_4$ samples after calcining at 950 °C. The inset shows the significant shift of the main peak (311) belonging to cubic spinel ferrite phase towards higher degree ($2\theta^\circ$) with increasing Co content

into the ferrite matrix led to the development of the hematite phase. The inset in Fig. 1 demonstrates there is a noticeable shift of the primary (311) peak for cubic phase spinel ferrite towards higher degrees ($2\theta^\circ$) when the cobalt substitution ratio increases. The observed phenomenon may be attributed to the comparatively greater ionic radius of cadmium (0.97 Å) in comparison to cobalt (0.74 Å) [22, 23]. Additionally, as seen in Fig. 1, it can be observed that the volume percentage of the hematite phase decreases as the doping concentration increases. This trend continues until it reaches sample $x = 1$, at which point the hexagonal phase completely disappears.

Rietveld refinements of the diffraction pattern [24] were performed on all samples, as seen in Fig. 2. These refinements proved the presence of two phases in the samples: the hexagonal $\alpha\text{-Fe}_2\text{O}_3$ phase with the space group R-3c and the cubic spinel phase with the space group Fd3m. The volume percentage of the $\alpha\text{-Fe}_2\text{O}_3$ phase decreased as the doping concentration increased, until it reached $x = 1$, at which point no further hexagonal phase was observed. The lattice parameter values of the cubic spinel phase were calculated using the FULL-PROF program, and these results are presented in Table 1. It is clear that the lattice constant decreases with an increase in the quantity of Co present. The relationship between the decrease in lattice parameters and the increase in doping content may be explained by considering the ionic radii of the impurity ions. The significant difference in ionic radii between Cd^{2+} (0.97 Å) and Co^{2+} (0.74 Å) [25] might be the primary factor contributing to this phenomenon.

Strain broadening and peak size contribute to the overall integral width of a Bragg peak. Williamson and Hall used

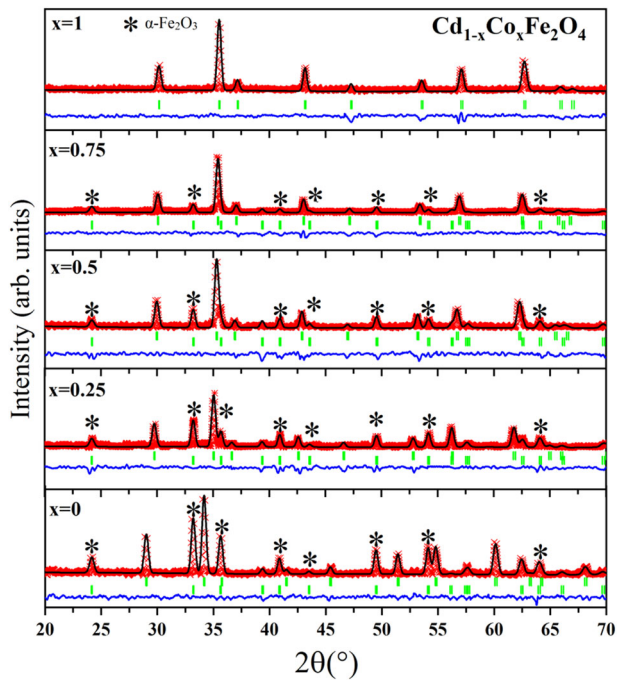


Fig. 2 Observed (symbols) and patterns calculated via Rietveld refinement (line) for all samples. Vertical bars indicate positions of Bragg reflection for the existing phases. The difference between calculated and observed intensities is shown at the bottom. The peaks associated with the impurity hematite phase are marked with asterisks

Table 1 Lattice parameter, particle size, lattice strain, dislocation density, theoretical density and hopping lengths L_A and L_B of prepared samples $Cd_{1-x}Co_xFe_2O_4$

$Cd_{1-x}Co_xFe_2O_4$	0.0	0.25	0.5	0.75	1.0
a (Å)	8.6835	8.4907	8.4311	8.4041	8.3796
D (nm)	61	64	65	78	83
ϵ	0.010	0.024	0.035	0.045	0.058
$\delta_L \cdot 10^{-4}$	2.7	2.5	2.4	1.6	1.5
ρ (gm/cm ³)	5.845	5.962	5.793	5.550	5.297
L_A (Å)	3.760	3.677	3.651	3.639	3.628
L_B (Å)	3.070	3.002	2.981	2.971	2.963

the different angle (θ) dependence of size and strain broadening to distinguish between these two parameters in their analysis [26, 27]. The Williamson-Hall formula is used here to determine how much strain is formed in nanocrystals as a result of lattice distortion and imperfection. By means of the uniform deformation model (UDM) described by Eq. (1), we have approximated the crystallite size and lattice strain of the $Cd_{1-x}Co_xFe_2O_4$ samples. The average crystallite size and lattice strain may be calculated using Eq. (1) [28] from the Williamson-Hall equation.

$$\beta_{hkl} \cos \theta = \frac{K \cdot \lambda}{D} + 4 \epsilon \sin \theta \quad (1)$$

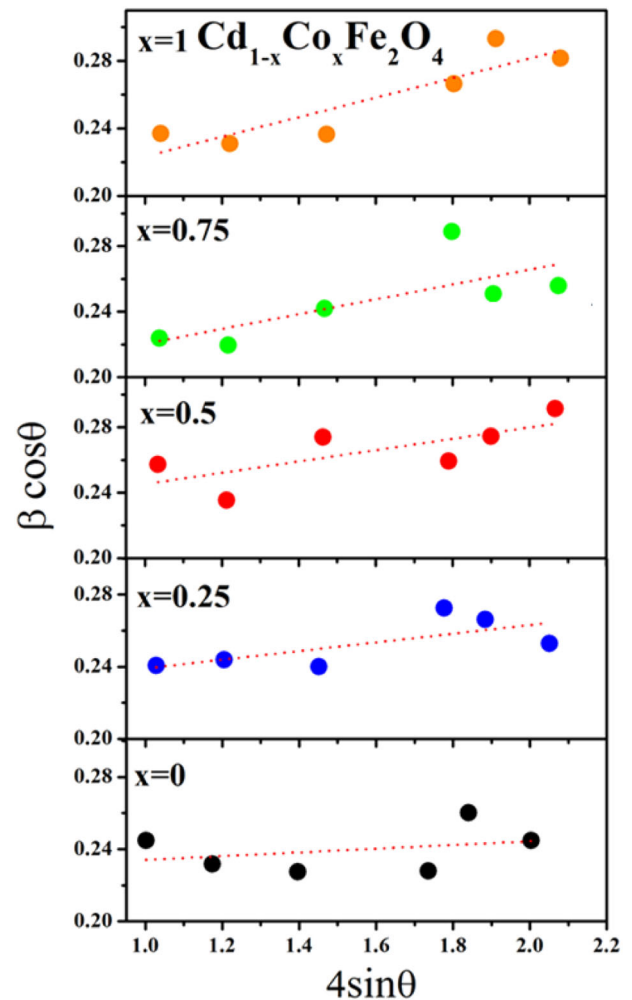


Fig. 3 a Williamson-Hall plot of $4\sin\theta$ against $\beta\cos\theta$ calculated from XRD spectra for the prepared samples $Cd_{1-x}Co_xFe_2O_4$

where D is the particle size in nanometers, λ is the wavelength, K is a constant (0.9), β_{hkl} is the peak width at half-maximum intensity and ϵ is the lattice strain. By plotting $4\sin\theta$ in the x -direction and $\beta_{hkl} \cos\theta$ in the y -direction, which is a linear fit as demonstrated in Fig. 3, the crystallite size and lattice strain may be determined. The average strain caused by the particles is represented by the slope of the figure, while the size of the nanocrystals is given by the intercept on the y -axis. According to Table 1, as Co concentration (x) rose, so did particle size and lattice strain.

The quality of the samples crystals is estimated by calculating the dislocation density δ_L . The δ_L values of $Cd_{1-x}Co_xFe_2O_4$ spinel nano ferrite was estimated using Eq. (2) [29]:

$$\delta_L = \frac{1}{D^2} \quad (2)$$

Table 1 indicate that the dislocation density δ_L decreased with increasing Co content (x). This behavior may be

related to the improvement of the crystallization process of Co doping; this in turn reduces the crystals defects of the synthesized samples.

The theoretical density ρ_x of $\text{Cd}_{1-x}\text{Co}_x\text{Fe}_2\text{O}_4$ samples was calculated using the relation (3) [30]:

$$\rho_x = \frac{8M}{N_A a^3} \quad (3)$$

where M is the molecular weight of the sample, N_A is Avogadro's number, and a is the lattice constant. Theoretical density ρ_x values for $\text{Cd}_{1-x}\text{Co}_x\text{Fe}_2\text{O}_4$ samples were found to decrease with increasing Co content (Table 1). The decline in theoretical density is attributed to the density convergence of Co (8.90 g/cm^3) and Cd (8.65 g/cm^3).

The lattice constant values were used to determine the hopping lengths L_A and L_B , which represent the distances between magnetic ions in the A site (Tetrahedral) and B site (Octahedral), respectively. These values were computed using relations (4, 5) and are shown in

Table 1.

$$L_A = \frac{a \times \sqrt{3}}{4} \quad (4)$$

$$L_B = \frac{a \times \sqrt{2}}{4} \quad (5)$$

Table 1 demonstrates that as the concentration of Co ions rises, the L_A and L_B decreases. The shrinking of the unit cell resulting from the conversion of larger ions into tetrahedral lattice sites and inclusion of smaller Co^{2+} ions into octahedral lattice sites may be identified as a result of this.

3.2 SEM and EDAX analysis

The surface morphological properties of the cadmium-cobalt ferrite samples were investigated using scanning electron microscopy (SEM). The majority of particles have been observed to possess a spherical shape and are found to be agglomerated, as seen in Fig. 4a. The substitution of cobalt

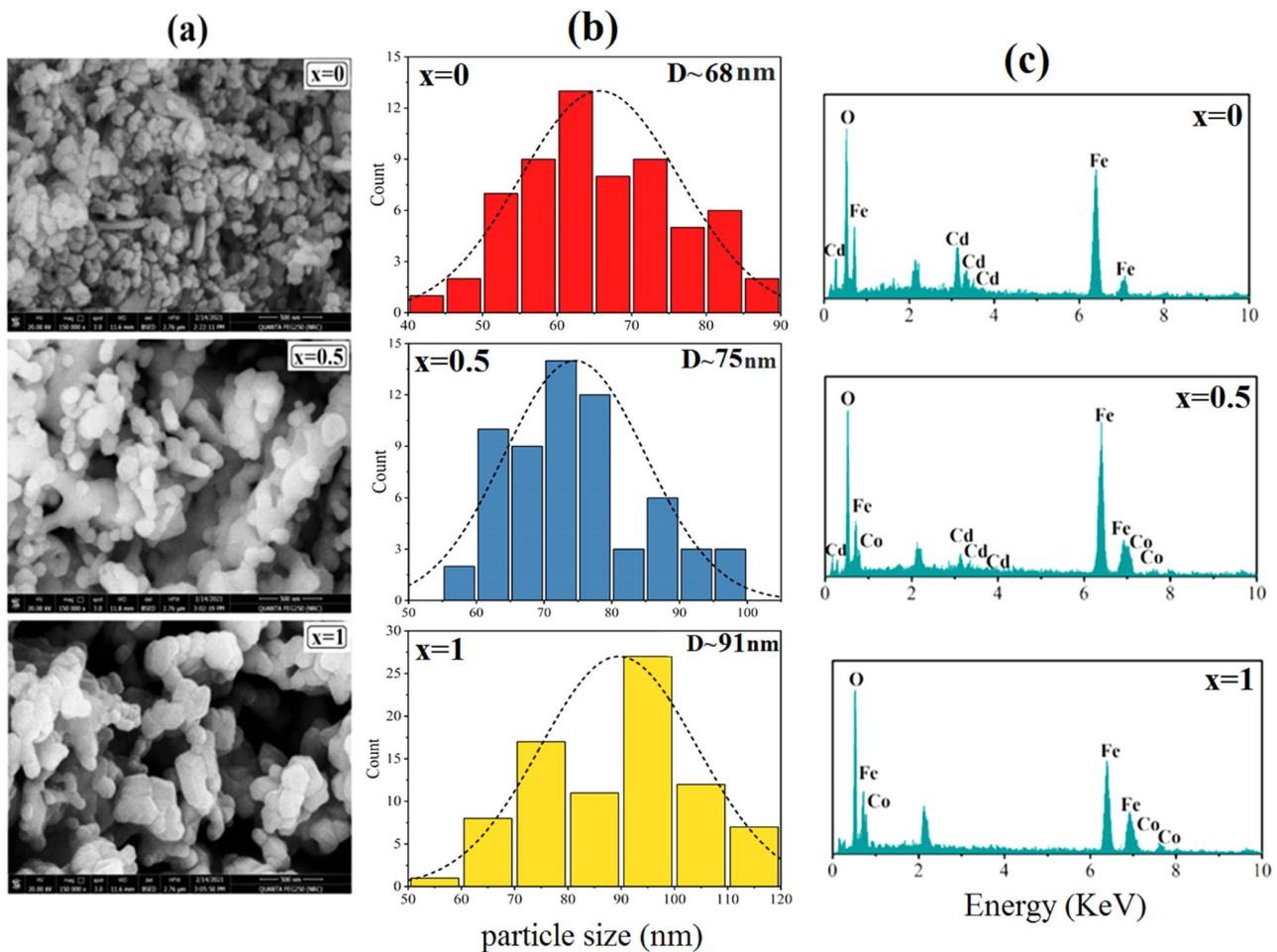


Fig. 4 a Scanning electron micrographs for the samples CdFe_2O_4 ($x=0$), $\text{Cd}_{0.5}\text{Co}_{0.5}\text{Fe}_2\text{O}_4$ ($x=0.5$) and CoFe_2O_4 ($x=1.0$) spinel ferrite. b Histogram distribution of particles size by using Image J software and (c) EDAX spectra of the $x=0$, 0.5 and $x=1.0$ samples

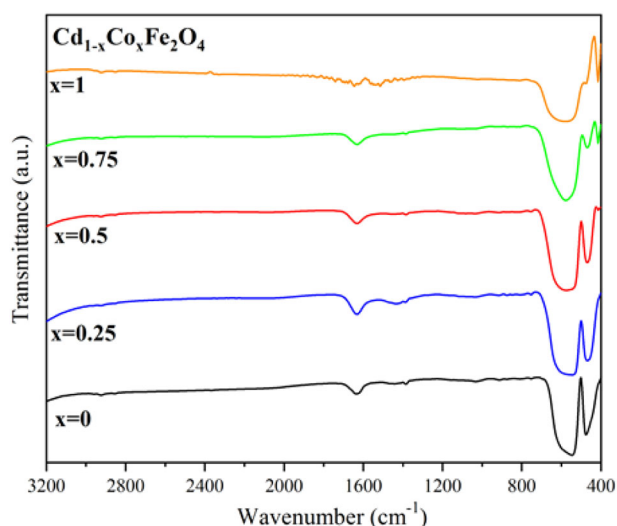
Table 2 EDX analysis of $\text{Cd}_{1-x}\text{Co}_x\text{Fe}_2\text{O}_4$ ($x = 0, 0.5$ and 1.0) samples

Sample	Element	wt%
$x = 0$	Fe	57.4
	Cd	12.7
	O	29.9
$x = 0.5$	Fe	55.5
	Cd	5.9
	O	22.5
	Co	16.1
$x = 1$	Fe	48.0
	O	25.7
	Co	26.3

has a significant influence on both the size and form of grains, which is readily observable. SEM images clearly demonstrated that the particle size increases with increasing Co-content (x) as revealed in histogram distribution of particles size (Fig. 4b), which is consistent with crystal size results from XRD analysis. Figure 4c shows that the samples' energy-dispersive X-ray (EDAX) spectra only showed emission peaks corresponding to the expected elements; there were no other contaminants that could be seen and the corresponding weight percent for each elements are listed in Table 2.

3.3 FTIR analysis

Fourier transform infrared spectroscopy (FTIR) is a very useful spectroscopic method for characterizing different functional groups inside materials. FTIR spectra were obtained in the range of $400\text{--}4000\text{ cm}^{-1}$, as seen in Fig. 5. The metal-oxygen bonds exhibit prominent peaks at wavenumbers of $559\text{--}588\text{ cm}^{-1}$ and $471\text{--}477\text{ cm}^{-1}$, which are indicative of the bonding typically seen in ferrite materials. According to Waldron [31], it can be shown that these peaks correspond to the stretching vibrations of the M-O species. Specifically, the bands within the range of $560\text{--}590\text{ cm}^{-1}$ are attributed to tetrahedral sites (A) (ν_t), while those within the range of $470\text{--}480\text{ cm}^{-1}$ are ascribed to octahedral sites (B) (ν_o). Table 3 shows the changes in wavenumber observed at sites (A) (ν_t), and (B) (ν_o) as the concentration of cobalt (Co) rises. It is remarkable that ν_t exceeds ν_o as a result of a higher degree of $\text{Fe}^{3+}\text{--O}^{2-}$ overlapping occurring at A sites compared to B sites. The difference in $\text{Fe}^{3+}\text{--O}^{2-}$ distances for the A and B sublattices controls the positioning of these two absorbance bands [20]. Moreover, the observed rise in (ν_t), values and decline in (ν_o), values when Co^{2+} ions are substituted is attributed to the preference of nonmagnetic divalent Cd^{2+} ions to occupy tetrahedral sites, hence compelling Fe and Co ions to occupy octahedral sites. Based on the

**Fig. 5** FTIR spectra for the prepared samples $\text{Cd}_{1-x}\text{Co}_x\text{Fe}_2\text{O}_4$ **Table 3** Variations of tetrahedral (ν_t) and octahedral (ν_o) stretching vibrations and force constants k_t and k_o of $\text{Cd}_{1-x}\text{Co}_x\text{Fe}_2\text{O}_4$ spinel ferrite nanoparticle samples

x	ν_t cm^{-1}	ν_o cm^{-1}	k_t $(\text{Dyne/cm}^1)*10^5$	k_o $(\text{Dyne/cm}^1)*10^5$
0.0	560	478	2.895	2.108
0.25	568	476	2.979	2.092
0.5	575	474	3.052	2.074
0.75	579	472	3.095	2.057
1.0	582	469	3.127	2.031

observation that Fe^{3+} and Co^{2+} ions possess smaller ionic radii compared to Cd^{2+} , it can be inferred that this difference leads to a reduction in the Fe-O bond length. Consequently, this structural modification induces a displacement of the (ν_t) towards higher energy and a corresponding shift of the (ν_o) towards lower energy.

The ionic force constants (K_T) and (K_O) associated with A sites and B sites, respectively, may be determined by substituting the values of vibrational frequencies (ν_t) and (ν_o) into the following Eq. (6) [32]

$$K = 4\pi^2 C^2 \nu^2 m \quad (6)$$

where c is the light speed ($3 \times 10^{10}\text{ cm/s}$), ν is the wavenumber at A and B sites, and m is the reduced mass of Fe^{3+} and O^{2-} ($2.601 \times 10^{-23}\text{ g}$). Table 3 lists the values for the force constants (K_T) and (K_O); note that as the Co content rises, the (K_T) values rise while the (K_O) values decline. Nonmagnetic divalent Cd^{2+} ions with a larger ionic radius preferentially occupy the tetrahedral sites, whereas the smaller Fe and Co ions occupy the octahedral sites, as seen by the increase in (K_T) and decrease in (K_T).

3.4 Magnetic properties

Hysteresis loops of spinel ferrites $\text{Cd}_{1-x}\text{Co}_x\text{Fe}_2\text{O}_4$ samples estimated in room-temperature fields of 20 kOe are shown in Fig. 6. The magnetic characteristics were enhanced by increasing the Co concentration and normal (S)-shaped curves were seen for all compositions, demonstrating their ferromagnetic nature. Saturation magnetization (M_s) and magnetic coercivity (H_c) are listed in Table 4 which demonstrates the changes brought about by the various Co substitutions. According to Néel's two sublattice models, there are three kinds of exchange activities (A-A, A-B, and B-B). Among those three, the A-B exchange is much stronger than the other two couplings. When the density of the cations and the magnetic moments of the cations are varied, the interchange between the magnetic ions will change. Substituting a trace quantity of Co^{2+} (B position) ions for Fe^{3+} (B position) will lead to an increase in the concentration of Fe^{3+} . By increasing the Co substitution ratio, the M_s value of the sample CoFe_2O_4 (pure cobalt) was raised from 13.31 emu/g (the value for undoped CdFe_2O_4) to 78.45 emu/g. Possible explanations include the exchange of magnetic Co^{2+} ions ($3 \mu_B$) for diamagnetic Cd^{2+} ions ($0 \mu_B$) [33]. In addition, the Magneto-crystalline anisotropy is enhanced by the incorporation of soft magnetic Co^{2+} ions, enabling samples to retain their magnetic ordering and display soft ferrimagnetic behavior.

Using the following relationships (7) and (8), the magnetic moment μ_B per formula unit in Bohr magneton (B) and the anisotropy constant K can be calculated [32, 34]:

$$\mu = \frac{M_s \times M_w}{5585} \quad (7)$$

$$K = \frac{M_s \times H_c}{0.98} \quad (8)$$

where M_s is the saturation magnetization, M_w is the molecular weight of the sample and H_c is the coercivity of the sample.

The correlation between the concentration of Co and the magnetic moment (μ_B) of the Bohr magneton is illustrated in Table 4. The enhancement of magnetic parameters can be attributed to the high extent of occupancy of the tetrahedral A-site by the Cd^{2+} ion [35, 36]. In contrast, the octahedral B-site is occupied by the Co^{2+} ion [37], and both the tetrahedral and octahedral sites are occupied by the Fe^{3+} ions. According to Néel's two sub-lattice models [38], the introduction of magnetic divalent ions (Co^{2+} ions) into ferrites results in an increase in the quantity of Fe^{3+} ions at the A-site and a decrease in the quantity of Cd^{2+} ions. This substitution accounts for the observed enhancements in saturation magnetization and magnetic moment. The migration of Fe^{3+} ions from the octahedral site (B-site) to the A-site is equivalent to

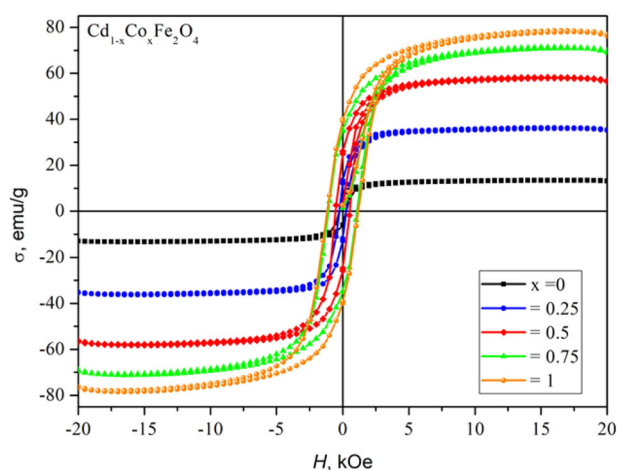


Fig. 6 Room temperature hysteresis loops for spinel ferrites samples $\text{Cd}_{1-x}\text{Co}_x\text{Fe}_2\text{O}_4$ obtained in ± 20 kOe field ranges

Table 4 Magnetic parameters of $\text{Cd}_{1-x}\text{Co}_x\text{Fe}_2\text{O}_4$ spinel ferrite nanoparticle samples

$\text{Cd}_{1-x}\text{Co}_x\text{Fe}_2\text{O}_4$	0.0	0.25	0.5	0.75	1.0
M_s (emu/g)	13.31	36.23	58.22	71.29	78.45
M_r (emu/g)	6.4075	13.203	25.927	35.360	39.988
H_c (Oe)	220.35	257.90	534.60	1092.6	1176.1
μ (μ_B)	0.687	1.782	2.724	3.165	3.296
K (erg/cm ³)	2992.71	9534.41	31759.60	79482.53	94147.20

the occupancy of Co^{2+} ions at the B-site. Consequently, as the concentration of Co^{2+} ions increases, the magnetic moment of the B-site sublattice diminishes, while the magnetic moment of the A-site sublattice increases with the addition of Fe^{3+} ions. Furthermore, the observed increase in saturation magnetization (M_s) was attributed to the enhanced super-exchange interaction within the inter-sub-lattice (A-B). This finding is consistent with the collinear two-sub-lattice model. The magneto-crystalline anisotropy of nanoparticles influences their H_c value [39]. As presented in Table 3, the H_c of the prepared samples increased as the Co^{2+} content increased. Strong spin-orbit coupling was associated with the high magnetocrystalline anisotropy of Co^{2+} ions; this could be attributed to the unquenched orbital moment of Co^{2+} ions in the asymmetric crystalline field of octahedral sites [40, 41]. Co^{2+} and Fe^{3+} had d-shell electron configurations of $3d^5$ and $3d^6$, respectively. Fe^{3+} ions possessed half-full electron shells, or five unpaired electrons, which led to orbital quenching ($L=0$). In this particular case, spin-orbit interactions are essentially negligible. In contrast, Co^{2+} ions possessed four unpaired electrons, and due to spin-orbit interactions, the orbital angular momentum remained unquenched. As a result, cobalt ions exhibited a greater degree of magneto-crystalline

Table 5 Cation distribution, ionic radius of the tetrahedral A (r_A), octahedral B site (r_B), theoretical lattice parameter (a_{th}) and Yafet–Kittel angle (α_{Y-K}) of $Cd_{1-x}Co_xFe_2O_4$

x	Cation distribution		r_A (Å)	r_B (Å)	a_{th} (Å)	α_{Y-K} (degree)
	A site	B site				
0.0	$Cd_{0.988}Fe_{0.012}$	$Cd_{0.012}Fe_{1.988}$	0.946	0.651	8.7412	85.65
0.25	$Cd_{0.742}Co_{0.118}Fe_{0.14}$	$Cd_{0.008}Co_{0.132}Fe_{1.86}$	0.875	0.652	8.6331	72.99
0.5	$Cd_{0.494}Co_{0.246}Fe_{0.26}$	$Cd_{0.006}Co_{0.254}Fe_{1.74}$	0.803	0.653	8.5250	59.78
0.75	$Cd_{0.247}Co_{0.363}Fe_{0.39}$	$Cd_{0.003}Co_{0.387}Fe_{1.61}$	0.731	0.654	8.4168	47.66
1.0	$Co_{0.46}Fe_{0.54}$	$Co_{0.54}Fe_{1.46}$	0.659	0.655	8.3086	34.32

anisotropy in comparison to iron ions. As a result, H_c increased in $Cd_{1-x}Co_xFe_2O_4$ samples [42].

3.5 Cation distribution

The examination of cation distribution in spinel ferrite provides valuable insights for the development of materials with specific features. The phenomenon of cation distribution refers to the arrangement of cations at tetrahedral (A) and octahedral (B) positions inside a crystal lattice. The determination of cation distribution in spinel ferrite may be achieved by the examination of XRD patterns and magnetic characteristics.

The enhancement of magnetic moment η_B , which arises from the progressive Co substitution ratio, may be elucidated by using the three-sublattice model proposed by Yafet and Kittel (Y-K model) [43, 44]. Based on the Y-K model, it is postulated that the B lattice may be partitioned into two distinct sublattices, namely B_1 and B_2 . These sublattices exhibit magnetic moments of similar magnitude, and each is oriented in an opposing canting direction at an identical angle. The two sublattices, B_1 and B_2 , have a triangular spin configuration that becomes more prominent as the concentration varies. The cation distribution of the spinel ferrite $Cd_{1-x}Co_xFe_2O_4$, as produced using the described method, is listed in Table 5. The most accurate assessment of cation distribution is obtained by comparing experimental lattice parameters acquired by X-ray diffraction with estimated lattice parameters derived from cation distribution.

The mean ionic radius of the tetrahedral A (r_A) and octahedral B site (r_B) can be calculated from Eqs. (9) and (10).

$$r_A = C_{A(Mn)}r_{Mn^{2+}} + C_{A(Cd)}r_{Cd^{2+}} + C_{A(Fe)}r_{Fe^{3+}} \quad (9)$$

$$r_B = \frac{1}{2} [C_{B(Mn)}r_{Mn^{2+}} + C_{B(Cd)}r_{Cd^{2+}} + C_{B(Fe)}r_{Fe^{3+}}] \quad (10)$$

In addition, the theoretical lattice parameter (a_{th}) was estimated by using the following Eq. (11) [45, 46]:

$$a_{th} = \frac{8}{3\sqrt{3}} [(r_A + R_o) + \sqrt{3}(r_B + R_o)] \quad (11)$$

where R_o is the ionic radius of oxygen. Table 5 provides the cation distribution and computed r_A , r_B for both tetrahedral

and octahedral positions for the prepared $Cd_{1-x}Co_xFe_2O_4$ spinel nanoparticles. The increase in the theoretical lattice parameter (a_{th}) as the Co content rises is illustrated in Table 5. Additionally, the similarity between the experimental and theoretical values for the lattice parameter verifies the cation distribution's validity.

The observation of the cation distribution and the correlation between the magnetic moment and the concentration of Co can be achieved through the calculation of the Y-K angle (α_{Y-K}). Equation (12) represents the magnetic moment $\mu_B(th)$ following the Y-K model.

$$\mu_B(th) = \mu_B \cos(\alpha_{Y-K}) - \mu_A \quad (12)$$

The magnetic moments on the A and B sites are denoted as μ_A and μ_B , respectively, and are given in units of Bohr magneton. It also demonstrates the agreement between the experimental and theoretical magnetic moment values, confirming the accuracy of the cation distribution. The values of α_{Y-K} angles as a function of x are presented in Table 5. The values of α_{Y-K} angles of $Cd_{1-x}Co_xFe_2O_4$ spinel ferrite exhibited a reduction as the concentration of Co increased.

3.6 Dielectric properties

The dielectric and electrical characteristics of the $Cd_{1-x}Co_xFe_2O_4$ samples, where x = 0, 0.25, 0.5, 0.75, and 1, were investigated over the frequency range from 10^{-1} to 10^7 Hz. Figure 7 illustrates the frequency dependence of the dielectric constant, usually called permittivity and denoted as ϵ' , for nano-composite samples of $Cd_{1-x}Co_xFe_2O_4$. The Cd-free sample has the lowest values for both permittivity and ac conductivity across the whole frequency range that was studied. This means that pure cobalt ferrite is more insulating than the other four samples that were investigated. This may explain the reduction of dielectric constant with increasing the concentration of cobalt. Permittivity rises very little with decreasing frequency; however, this sample shows exceptional stability with respect to frequency. The figure represents a superposition polarization of the dipoles in the Cd-free samples and the other three composites, which is the result of charge transfer between divalent and trivalent cations inside the spinel structure and

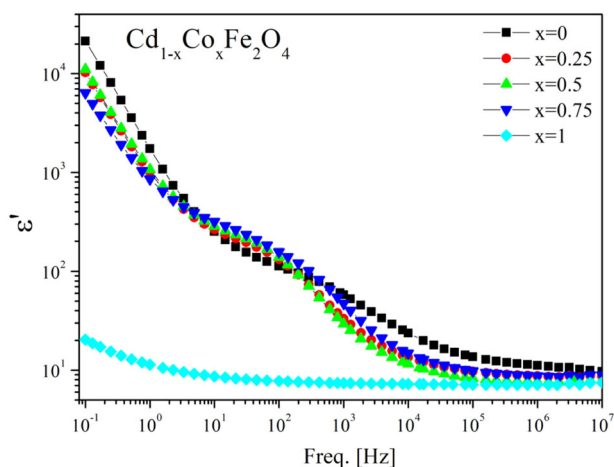


Fig. 7 Dielectric constant (ϵ') as a function of frequency for all compositions under investigations, $\text{Cd}_{1-x}\text{Co}_x\text{Fe}_2\text{O}_4$ with $x = (0, 0.25, 0.5, 0.75, 1)$ sintered at 950°C

the contribution of charge carriers' movement. Spinel ferrite's dielectric spectra provide important details regarding the movement of electric charge carriers and the process of polarization in ferrites. As seen in Fig. 7, the frequency dependence of ϵ' , for the four samples exhibits three distinct tendencies. The observed linear drop in conductivity at lower frequencies may be attributed to the movement of free-charge carriers. This behavior may be followed by a plateau-like pattern in the presentation of dc-conductivity. In this case, we see a bending-like behavior in the middle-frequency band (from around 5 Hz to roughly 10 kHz). This deflection is likely caused by Maxwell–Wagner–Sillars (MWS) polarization at the interface. In recent years, this kind of polarization in inhomogeneous structures has gained well-known recognition [47–49].

The formation of interfacial polarization in a given material occurs due to the presence of conducting grains that are separated by non-conducting grain boundaries. The emergence of a network of microcapacitors exhibiting electric energy storage capabilities is a very promising characteristic seen in nanocomposites [50]. The phenomenon of interfacial polarization, which affects the dielectric constant, exhibits a gradual decrease as the frequency increases. At higher frequencies beyond a specific threshold (approximately 10 kHz in this study), the exchange of electrons between Fe^{3+} and Fe^{2+} ions is unable to keep up with the alternating field, resulting in a constant value [51–54]. The addition of cobalt to pure cadmium ferrite results in a significant rise in permittivity.

The dielectric loss (ϵ'') exhibits an analogous behavior, as depicted in Fig. 8, which supports the concept that the real (ϵ') and imaginary (ϵ'') components of the complex dielectric function are not independent. The observed phenomenon of the dielectric characteristics of the various samples exhibiting a pronounced decline as the frequency

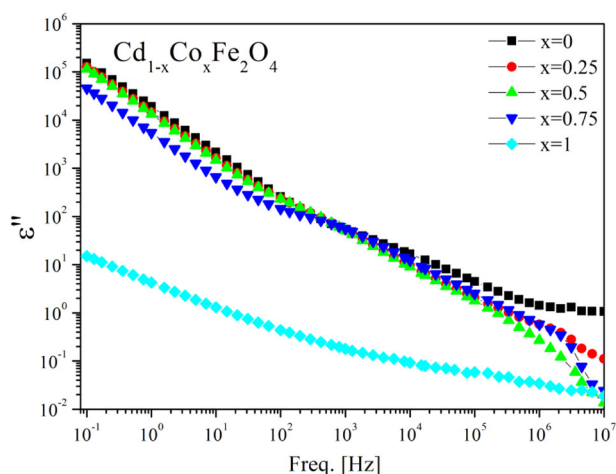


Fig. 8 Dielectric loss (ϵ'') as a function of frequency for all compositions under investigations, $\text{Cd}_{1-x}\text{Co}_x\text{Fe}_2\text{O}_4$ with $x = (0, 0.25, 0.5, 0.75, 1)$ sintered at 950°C

rises may be attributed to the influence of conductivity. This observation validates the governing equation that delineates the correlation between the complex conductivity and dielectric function.

The dielectric loss tangent, $\tan \delta$, often known as the dissipation factor, is a parameter that quantifies the rate at which energy is lost or dissipated in dielectric materials. The expression given in Eq. (13) represents the ratio between the dielectric constant, denoted as ϵ' , and the dielectric loss, denoted as ϵ'' .

$$\tan \delta = \frac{\epsilon''}{\epsilon'} \quad (13)$$

Figure 9 illustrates the frequency-dependent values of $\tan \delta$ for the Co compositions under investigation, which were sintered at a temperature of 950°C . The interfacial polarization exhibits a dynamic peak relaxation phenomenon at intermediate frequencies. Additionally, a more pronounced peak is seen at lower frequencies, indicating slower dynamic behavior. This lower frequency peak is indicative of the charge carriers' transit mechanism, including a hopping process. To clarify, the observed maximum in the slower dynamic of the hopping mechanism shown in the figure may be ascribed to the fortuitous alignment between the frequency of the applied electric field and the frequency at which charge carriers engage in hopping. This phenomenon is evident when the frequency of the applied electric field is lower than or similar to the frequency at which charge carriers transition between Fe^{2+} and Fe^{3+} ions. At elevated frequencies, the behavior of hopping electrons and the modification of MWS-polarization deviate from their response to the electric field, resulting in a reduction in $\tan \delta$ and the attainment of stability.

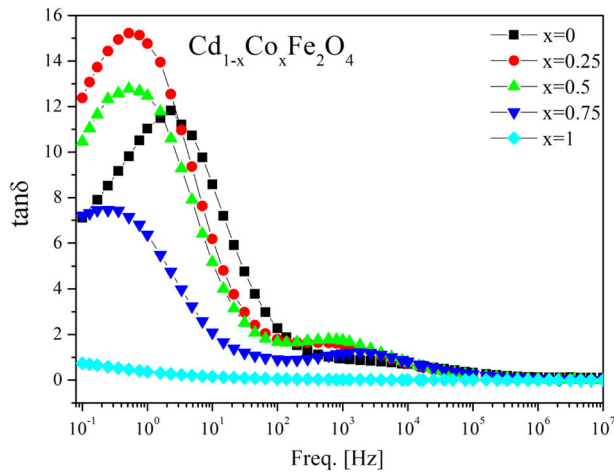


Fig. 9 Dielectric loss tangent, $\tan \delta$ as a function of frequency for $\text{Cd}_{1-x}\text{Co}_x\text{Fe}_2\text{O}_4$ under investigations

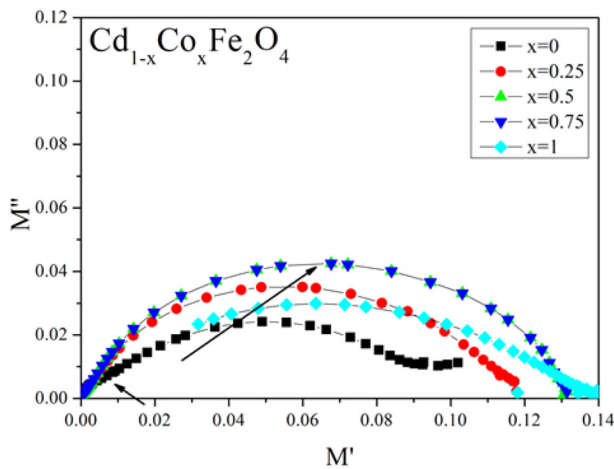


Fig. 10 The imaginary part of complex electric modulus as illustrated graphically against its real part (Nyquist plot) of the investigated samples as indicated

The real, M' , and imaginary, M'' , parts of the complex electric modulus can be estimated from those of the complex permittivity by using Eqs. (14, 15):

$$M' = \frac{\epsilon'}{(\epsilon'^2 + \epsilon''^2)} \quad (14)$$

$$M'' = \frac{\epsilon''}{(\epsilon'^2 + \epsilon''^2)} \quad (15)$$

The determination of the electric modulus facilitates the analysis of the relaxation phenomenon. Figure 10 displays the Nyquist plot, $M''(M')$, for the investigated samples. A representation of the relaxation resulting from the grain boundary contribution is shown by a semi-circular arc, taking into account the scale of the figure. Upon careful

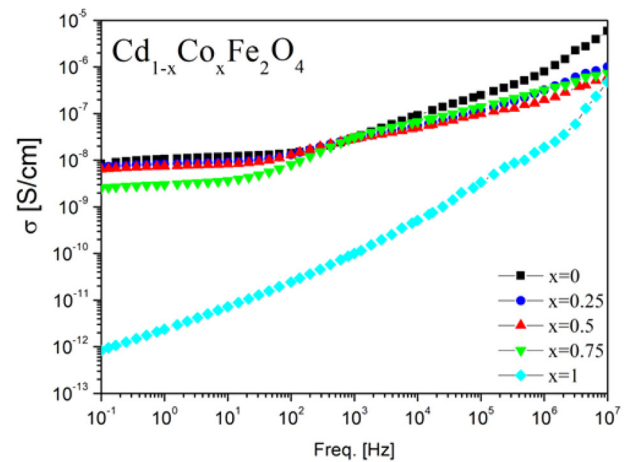


Fig. 11 Real part of the complex conductivity, σ' , vs. frequency for all compositions under investigations

examination of the Figure, it becomes evident that there is a discernible shoulder-like characteristic seen in the lower range of M' (specifically, at higher frequencies). The Nyquist plot of the complex electric modulus, denoted as $M^* = M' + M''$, is often used to provide precise insights into the conduction process occurring inside grain or grain borders. At higher frequencies, the presence of a shoulder indicates the resistance of grains only. Conversely, the arc seen over a wider range of frequencies represents the combined resistance of both grains and grain boundaries [55].

Figure 11 shows the real part of the complex conductivity, denoted as σ' , plotted against frequency for the five samples that were being studied in their original state. The graphic clearly illustrates two distinct tendencies. In the higher frequency range, there is a progressive rise in the ac conductivity as the frequency increases. This increase of ac conductivity, σ' , is generally linear on the log-log plot and follows a power law (that is: $\sigma' = k\omega^n$, where k and n are constants and ω is the radial frequency [56]).

When σ' characterized on the low frequency side by a plateau, its value directly yields the dc conductivity, σ_{dc} , and the characteristic frequency, ν_c , at which dispersion sets in and turns into a power law at higher frequencies. However, in this case, the frequency dependence of ac conductivity follows the well-known Jonscher power law. However, in our case, and according to the heterogeneous structure, there a clear effect of the interfacial polarization that originated from the accumulation of charge carriers at the grain boundaries. So, it is not possible to fit the data using Jonscher's model within an acceptable error.

The predominant source of electrical conductivity in ferrites is often attributed to the phenomenon of electron hopping between ions of the same element that exist in various valence states. The elevated concentrations of Co^{2+} result in the displacement of a greater number of Fe^{2+} ions, thereby

leading to a decrease in conductivity. The introduction of an alternating current (AC) field results in an increase in electron hopping, hence enhancing the AC conductivity. Nevertheless, the departure from linearity shown in the data may be attributed to the presence of interfacial polarization, often referred to as Maxwell-Wagner-Sillier polarization. This phenomenon arises due to the buildup of charge carriers at the interfaces. The electrical responsiveness of the system is affected by the migration of charges in response to an applied alternating current (AC) field. In the lower frequency range, the ac-conductivity is less affected by or even doesn't depend on the frequency of the applied external field at a specific characteristic frequency (ν_c).

The equation consists of two distinct elements. The first element, referred to as dc-conductivity (σ_{dc}), is independent of frequency and arises from band conduction. The subsequent element, known as ac-conductivity (σ_{ac}), is frequency-dependent and arises from electron hopping at the B-site. It is important to observe that the rise in σ_{dc} is followed by a steady increase in ν_c . The empirical Barton-Nakajima-Namikawa (BNN) connection suggests a linear correlation between the two parameters, with the relation $\sigma_{dc} \sim \nu_c$ [57, 58]. It may be inferred that an increase in the characteristic frequency results in an increase in conductivity. Considering the reciprocal relationship between frequency and time, there exists an inverse relationship between the duration of time and the level of conductivity, so that shorter durations correspond to greater levels of conductivity. This observation provides evidence that the measured time is uniquely attributable to the ion's hopping time.

4 Conclusion

Co-substituted CdFe_2O_4 nanocrystalline spinel ferrites were successfully synthesized using the flash auto-combustion method. Based on the X-ray diffraction data, it can be shown that the analyzed samples have a cubic-phase spinel ferrite structure, which corresponds to the Fd-3m space group. The lattice parameters exhibited a reduction, accompanied by a rise in both particle size and lattice strain, as the Co concentration (x) increased. According to scanning electron microscopy (SEM) images, it has been seen that the majority of the particles have a spherical shape and are found to be agglomerated. The FTIR analysis successfully identified two main vibrational modes linked to the stretching of metal-oxygen bonds in the tetrahedral and octahedral sites. This confirmed that the synthesized ferrites have a spinel structure. The magnetic measurements demonstrate an enhancement in many properties, such as saturation magnetization (M_s), remanence magnetization (M_r), coercivity (H_c), and magnetic moment (μ_B), with an increase in the Co substitution content. The permittivity for

the composition $\text{Cd}_{1-x}\text{Co}_x\text{Fe}_2\text{O}_4$ as sintered at 950 °C exhibits a frequency dependency that indicates the formation of a net of micro capacitors-like behavior in the former. This is due to the efficiently conducting grains being separated from one another by a thin layer of weakly conducting grain boundaries. The compositions' conductivity spectra display two distinct trends that are divided by a characteristic frequency.

Data availability

No datasets were generated or analysed during the current study.

Funding MH Nasr, AS Abouhaswa, and AA EL-Hamalawy performed all the experimental work (sample preparation and its characterization) and prepared manuscript. Gamal M Turkey performed the dielectric measurements and its discussion. MM Elkholy, LMS El-Deen and M. Moustafa helped significantly in the explanation and discussion of experimental results.

Compliance with ethical standards

Conflict of interest The authors declare no competing interests.

References

1. Ibrahim AM, El-latif MMA, Mahmoud MM (2010) Synthesis and characterization of nano-sized cobalt ferrite prepared via polyol method using conventional and microwave heating techniques. *J Alloys Compd.* 506:201–204
2. Azam A (2012) Microwave assisted synthesis and characterization of Co doped Cu ferrite nanoparticles. *J Alloys Compd.* 540:145–153
3. Balavijayalakshmi J, Suriyanarayanan N, Jayaprakash R, Gopalakrishnan V (2013) Effect of concentration on dielectric properties of Co-Cu ferrite nano particles. *Phys. Procedia* 49:49–57
4. Padhan AM, Rajaiitha PM, Nayak S, Hajra S, Sahu M, Jagličić Z, Koželj P, Kim HJ (2023) Synthesis and application of mixed-spinel magnesioferrite: structural, vibrational, magnetic, and electrochemical sensing properties. *Mater Chem Front* 7:72–84
5. Nayak S, Ghorai S, Padhan AM, Hajra S, Svedlindh P, Murugavel P (2022) Cationic redistribution induced spin-glass and cluster-glass states in spinel ferrite. *Phys Rev B* 106(17):174402
6. KN Trohidou Magnetic Nanoparticle Assemblies, Pan Stanford, 2014.
7. Oh Y, Sahu M, Hajra S, Padhan AM, Panda S, Kim HJ (2022) Spinel ferrites (CoFe_2O_4): synthesis, magnetic properties, and electromagnetic generator for vibration energy harvesting. *J Electron Mater* 51:1933–1939
8. Rajaiitha PM, Hajra S, Sahu M, Mistewicz K, Toroń B, Abolhassani R, Panda S, Mishra YK, Kim HJ (2022) Unraveling highly efficient nanomaterial photocatalyst for pollutant removal: a comprehensive review and future progress, *Materials Today. Chemistry* 23:100692
9. Godlyn Abraham A, Manikandan A, Manikandan E, Vadivel S, Jaganathan SK, Baykal A, Renganathan PS (2018) Enhanced magneto-optical and photo-catalytic properties of transition metal cobalt (Co^{2+} ions) doped spinel MgFe_2O_4 ferrite nanocomposites. *J Magn Magn Mater* 452:380–388

10. Manikandan A, Judith Vijaya J, John Kennedy L (2013) Comparative investigation of NiO nano- and microstructures for structural, optical and magnetic properties. *Phys E* 49:117–123
11. Maruthamani D, Vadivel S, Kumaravel M, Saravanakumar B, Bappi P, Sankar Dhar S, Habibi-Yangjeh A, Manikandan A, Ramadoss G (2017) Fine cutting edge shaped Bi₂O₃ rods/reduced graphene oxide (RGO) composite for supercapacitor and visible-light photocatalytic applications. *J Colloid Interface Sci* 498:449–459
12. Asiri S, Sertkol M, Guner S, Gungunes H, Batoo KM, Saleh TA, Sozeri H, Almessiere MA, Manikandan A, Baykal A (2018) Hydrothermal synthesis of Co_yZn_yMn_{1-2y}Fe₂O₄ nanoferrites: Magneto-optical investigation. *Ceram. Int.* 44:5751–5759
13. Mathubala G, Manikandan A, Arul Antony S, Ramar P (2016) Enhanced photocatalytic activity of spinel Cu_xMn_{1-x}Fe₂O₄ nanocatalysts for the degradation of methylene blue dye and optomagnetic properties. *Nanosci Nanotechnol Lett* 8:375–381
14. Maaz K, Duan JL, Karim S, Chen YH, Zhai PF, Xu LJ, Yao HJ, Liu J (2016) Fabrication and size dependent magnetic studies of Ni_xMn_{1-x}Fe₂O₄ (x = 0.2) cubic nanoplates. *J Alloys Compd.* 684:656–662
15. Abdallah HMI, Moyo T (2014) Superparamagnetic behavior of Mn_xNi_{1-x}Fe₂O₄ spinel nanoferrites. *J Magn Magn Mater* 361:170–174
16. Dippong T, Levei EA, Deac IG, Petean I, Borodi G, Cadar O (2021) Sol-gel synthesis, structure, morphology and magnetic properties of Ni_{0.6}Mn_{0.4}Fe₂O₄ nanoparticles embedded in SiO₂ matrix. *Nanomaterials* 11:3455
17. Luo T, Hou X, Liang Q, Zhang G, Chen F, Xia Y, Ru Q, Yao L, Wu Y (2018) The influence of manganese ions doping on nanosheet assembly NiFe₂O₄ for the removal of Congo red. *J. Alloys Compd.* 763:771–780
18. Chakradhary VK, Ansari A, Jaleel Akhtar M (2019) Design, synthesis and testing of high coercivity cobalt doped nickel ferrite nanoparticles for magnetic applications. *J Magn Magn Mater* 469:674–680.
19. Chand P, Vaish S, Kumar P (2017) Structural, optical and dielectric properties of transition metal (MFe₂O₄; M= Co, Ni and Zn) nanoferrites. *Phys B* 524:53–63
20. Dippong T, Levei EA, Goga F, Petean I, Avram A, Cadar O (2019) The impact of polyol structure on the formation of Zn_{0.6}Co_{0.4}Fe₂O₄ spinel-based pigments. *J Sol-Gel Sci Technol* 92:736–744
21. Abushad A, Arshad M, Naseem S, Ahmed H, Ansari A, Chakradhary VK, Husain S, Khan W (2022) Synthesis and role of structural disorder on the optical, magnetic and dielectric properties of Zn doped NiFe₂O₄ nanoferrites. *J Mol Struct* 1253:132205
22. Pecharsky KV, Zavalij YP (2009) *Fundamentals of powder diffraction and structural characterization of materials* (2nd ed.). New York: Springer
23. Debnath S, Das A, Das R (2021) Effect of cobalt doping on structural parameters, cation distribution and magnetic properties of nickel ferrite nanocrystals. *Ceramics Int* 47:16467–16482
24. Rietveld HM (1969) A profile refinement method for nuclear and magnetic structures. *J Appl Cryst* 2:71–65
25. Shannon RD Revised effective ionic radii and systematic studies of interatomic distances in halides and chalcogenides, *Acta Crystallogr Sect. A.*
26. Mote VD, Purushotham Y, Dole BN (2012) Williamson-Hall analysis in estimation of lattice strain in nanometer-sized ZnO particles. *J Theor Appl Phys* 6:1
27. Kumar VK, Paramesh D, Reddy PV (2015) Effect of aluminium doping on structural and magnetic properties of Ni-Zn ferrite nanoparticles. *World J Nano Sci. Eng* 5:77–68
28. Kulkarni AB, Mathad SN (2018) Effect of sintering temperature on structural properties of Cd doped Co-Zn Ferrite. *J NanoElectron Phys* 10:01001.
29. Mohamed WS, Abu-Dief AM (2018) Synthesis, characterization and photocatalysis enhancement of Eu₂O₃-ZnO mixed oxide nanoparticles. *J Phys Chem Solids* 116:375–385
30. Akhter S, Paul DP, Abdul Hakim MD, Saha DK, Al-Mamun M, Parveen A (2011) Synthesis, structural and physical properties of Cu_{1-x}Zn_xFe₂O₄ Ferrites. *Mater Sci Appl* 2:1675–16
31. Waldron RD (1955) Infrared spectra of ferrites. *Phys Rev* 99:1727–1735
32. Phor L, Chahal S, Kumar V (2020) Zn²⁺ substituted superparamagnetic MgFe₂O₄ spinel-ferrites: investigations on structural and spin-interactions. *J Adv Ceram* 9(5):576–587
33. Li JG, Tian Q, Wang Q, Wang S, Zhang XD (2009) Structure and magnetic properties of Ni_{0.11}Zn_xCo_{0.03}Fe_{2.86-x}O₄ ferrite films deposited on Ag-coated glass substrates by wet chemical method. *Thin Solid Films* 518:313–318
34. Suman S, Chahal A, Kumar P (2020) Zn Doped α-Fe₂O₃: an efficient material for UV driven photocatalysis and electrical conductivity. *Curr Comput Aided Drug Des* 10:273–49
35. Meng F, Shang X, Zhang W, Zhang Y (2017) Effect of In³⁺ substitution on structural and magnetic properties of Ni ferrite nanoparticles. *Physica B* 504:73–69
36. Patil SA, Mahajan VC, Gadge AK, Lotake SD (1998) Structure and magnetic properties of Cd and Ti/Si substituted cobalt ferrites. *Mater Chem Phys* 57:86
37. Hemeda OM, Barakat MM (2001) Effect of hopping rate and jump length of hopping electrons on the conductivity and dielectric properties of Co–Cd ferrite. *J Magn Magn Mater* 223:127
38. Néel L, Néel L, Chem P, Louis N (1984) Magnetic properties of ferrites: ferrimagnetism and antiferromagnetism. *Phys Chem Earth Sci* 31:18
39. Tiwari R, De M, Tewari HS, Ghoshal SK (2020) Structural and magnetic properties of tailored NiFe₂O₄ nanostructures synthesized using auto-combustion method. *Results Phys* 16:1029162
40. Pulišová P, Kováč J, Voigt A, Raschman P (2013) Structure and magnetic properties of Co and Ni nano-ferrites prepared by a two-step direct microemulsions synthesis. *J Magn Magn Mater* 341:93–99
41. Varshney D, Verma K, Kumar A (2011) Substitutional effect on structural and magnetic properties of A_xCo_{1-x}Fe₂O₄ (A = Zn, Mg and x = 0.0, 0.5) ferrites. *J Mol Struct* 1006:447–452
42. Özgür Ü, Alivov Y, Morkoç H (2009) Microwave ferrites, part 1: fundamental properties. *J Mater Sci: Mater Electron* 20:789–834
43. Yafet Y, Kittel C (1952) Antiferromagnetic arrangements in ferrites. *Phys Rev* 87(2):290–294
44. Joshi GK, Khot AY, Savant SR (1988) Magnetisation, Curie temperature and YK angle studies of Cu substituted and non-substituted NiZn mixed ferrites. *Solid State Commun* 65:1593
45. Batoo K, Kumar Bhargava DG, Yang Y, Al-Douri Y, Singh M, Jotania R, Imran A (2017) “Structural, morphological and electrical properties of Cd²⁺ doped MgFe_{2-x}O₄ ferrite nanoparticles.”. *J Alloys Comp* 726:179–186
46. Amin N, Sajjad Ul Hasan M, Majeed Z, Latif Z, Ajaz Un Nabi M, Mahmood K, Ali A, Mehmood K, Fatima M, Akhtar M, Arshad M, Bibi A, Iqbal M, Jabeen F, Bano N (2020) Structural, electrical, optical and dielectric properties of yttrium substituted cadmium ferrites prepared by Co-Precipitation method. *Ceram Int* 46:20798–20809
47. Blundell S, Thouless D (2003) Magnetism in condensed matter. *Am J Phys* 71:94–95
48. Margha FH, El-Bassyouni GT, Turkey GM (2019) Enhancing the electrical conductivity of vanadate glass system (Fe₂O₃, B₂O₃,

- V₂O₅) via doping with sodium or strontium cations. *Ceram Int* 45:1183811843
49. Hegab NA, Bekheet AE, Afifi MA, Wahab LA, Shehata HA (2007) Effect of Cd addition on the AC conductivity and dielectric properties of Ge₇₀Te₃₀ films. *J Ovonic Res* 3:71–82
50. Ahmad R, Gul IH, Zarrar M, Anwar H, Niazi MB, Khan A (2016) Improved electrical properties of cadmium substituted cobalt ferrites nano-particles for microwave application. *J Magn Magn Mater* 405:28–35
51. Mahdy MA, El Zawawi I, Turkey GM (2019) Lead telluride nanocrystalline thin films: structure, optical characterization and a broadband dielectric spectroscopy study. *Curr Appl Phys* 19(7):787–793
52. Kumar A, Sharma P, Yang W, Shen J, Varshney D, Li Q (2016) Effect of La and Ni substitution on structure, dielectric and ferroelectric properties of BiFeO₃ ceramics. *J Ceram Int* 42:14805–14812
53. Farid HMT, Ahmad I, Ali I, Ramay SM, Mahmood A, Murtaza G (2017) Dielectric and impedance study of praseodymium substituted Mg-based spinel ferrites. *J Magn Magn Mater* 434:143–150
54. Nath S, Barik SK, Choudhary RNP, Barik SK (2017) Structural, dielectric and impedance characteristics of (Sm_{0.5}Li_{0.5})(Fe_{0.5}V_{0.5})O₃ multiferroics. *Phys Lett A*, 381:2174. 27
55. El-Mehalawy N, Awaad M, Turkey GM, Ali-Bik MW, Abd El Rahim SH, Naga SM (2021) Self-Glazing dielectric ceramic bodies fabricated from Egyptian rhyodacite and kaolin. *Mater Chem Phys* 270:124785
56. AS Abouhaswa, MH Badr, MH Nasr, MM Elkholy, LMS El-Deen, GM Turkey, M Moustafa, AA ELHamalawy, Investigation of crystal structure, electrical and magnetic properties of spinel Mn–Cd ferrite nanoparticles. *J Inorg Organomet Polym Mater* <https://doi.org/10.1007/s10904-021-02116-9> (2021).
57. El Hiti MA (1999) Dielectric behaviour in Mg–Zn ferrites. *J Magn Magn Mater* 192:305
58. Dhaou MH, Hcini S, Mallah A, Bouazizi ML, Jemni A (2017) Structural and complex impedance spectroscopic studies of Ni_{0.5}Mg_{0.3}Cu_{0.2}Fe₂O₄ ferrite nanoparticle. *Appl Phys A* 123:8

Publisher's note Springer Nature remains neutral with regard to jurisdictional claims in published maps and institutional affiliations.

Springer Nature or its licensor (e.g. a society or other partner) holds exclusive rights to this article under a publishing agreement with the author(s) or other rightsholder(s); author self-archiving of the accepted manuscript version of this article is solely governed by the terms of such publishing agreement and applicable law.